A compact dual-band bandpass filter based on porous silicon dual-microcavity of one-dimensional photonic crystal*

MA Hui (马辉) **and ZHANG Hong-yan** (张红燕)**
School of Physical Science and Technology, Xinjiang University, Urumqi 830046, China

(Received 8 January 2015)

We propose a compact dual-band bandpass filter (BPF) based on one-dimensional porous silicon (PS) photonic crystal by electrochemical etching. By inserting three periods of high and low reflective index layers in the center of porous silicon microcavity (PSM), two sharp resonant peaks appear in the high reflectivity stop band on both sides of the resonance wavelength. Through simulation and experiment, the physical mechanisms of the two resonance peaks and the resonance wavelength are also studied. It is found that the resonance wavelength can be tuned only by adjusting the effective optical thickness (EOT) of each PS layer, in which different resonance wavelengths have different widths between the two sharp resonance peaks. Besides, the analysis indicates that oxidization makes the blue shift become larger for high wavelength than that for low wavelength. Such a fabricated BPF based on PS dual-microcavity is easy to be fabricated and low cost, which benefits the application of integrated optical devices.
Document code: A **Article ID:** 1673-1905(2015)02-0095-5
DOI 10.1007/s11801-015-5006-1

Photonic crystals have attracted considerable attentions due to the periodically modulated dielectric functions, which results in the light propagation dramatically different from that in the bulk material[1], such as defect mode. Photonic bandgap causes the range of frequency in which the optical propagation is prohibited in any direction, and the defect mode allows modes to appear in photonic bandgap which is localized in the small volume around the defect. Many surveys have been studied, and these unique optical phenomenons play an important role in the miniaturization of photonic devices. In general, photonic devices are more compact and more sensitive than other optical devices, and they are suitable candidates for the realization of future passive and active optical devices[2,3], especially in the optical communication systems[4-6]. The muti-band filter as a key component for filtering the unwanted signals in radio frequency systems is necessary to generate two or more frequency bands, and it is the main device in optical communication systems. Contemporary studies on muti-band filters are mainly targeted to achieve ultra-compact and polarization insensitive devices with a low cross-talk ratio between output channels. So a considerable number of compact muti-band filters with different photonic crystal structures have been presented, such as fiber Bragg gratings, Fabry-Perot filters and arrayed waveguide gratings[7-9]. For the development of highly dense photonic integrated circuits, more compact muti-band filters using new materials and structures are necessary. By introducing a defect in photonic crystals, the photophysical properties of the photonic devices can produce new characteristics, and some new optical small-scale devices can be explored.

Nanoporous materials as a subset of nanomaterials are also scientific and technological important[10-12], because pores on the surface of nanoporous materials act as binding sites which are able to adsorb and interact with atoms, ions or molecules on their large interior surfaces. Silicon is an attractive and suitable material for commercial industry due to its ready availability and easy compatibility in modern integrated circuit (IC) industry and advanced electronic industry. There are some unique properties which are noticeable when the structure of silicon reduces to nano-dimension, such as porous silicon (PS). PS is one of the most promising nanomaterials due to its morphology[13-15]. It exhibits a very high surface to volume ratio (~800 $m^2 \cdot cm^{-3}$), and its surface containing nanocrystallites is like a quantum sponge, which allows the integration across a chip surface and the immobilization of more probe molecules compared with a flat surface. Furthermore, PS is a candidate of photonic structured material due to its tunable refractive index just by means of changing pore diameter or porosity in electrochemical etching[16,17]. Photonic crystals entirely based

* This work has been supported by the National Training Program of Innovation and Entrepreneurship for Undergraduate (No.201410755013), and the Foundation of Xinjiang Education (No.XJEDU2013S04).
** E-mail: zhy@xju.edu.cn

on silicon hope to be further used for light emitting devices, transistors, solar cells, industrial sensors, integrated circuits and many other high applications. So the proposed muti-band filter based on PS has potential commercial applications in future photonic integrated circuits.

In this paper, through simulations and experiments, a compact dual-band bandpass filter (BPF) based on one-dimensional (1D) PS photonic crystal is constructed, and its reflectance characteristics are discussed. In simulation, three periods of high and low refractive index layer are inserted in the center of porous silicon microcavity (PSM,) and two sharp resonant peaks appear in high reflectivity stop band. The effects of tuning resonance wavelength are shown by changing the effective optical thickness (EOT) of PS layer for 1D PS photonic crystal. Just as expected, the resonance wavelengths of two oxidized resonance peaks are located separately at 1 300 nm and 1 400 nm from experiments, which are very close to the optical communication wavelengths.

Fig.1(a) shows a schematic diagram of PSM following $(LH)^6L_c(HL)^6$ sequence, where H represents high refractive index (low porosity) PS layer, and L and L_c represent low refractive index (high porosity) PS layers. A microcavity consists of a central defect layer, which is sandwiched between two distributed Bragg reflectors (DBRs). Each DBR is composed of periodic multilayers with an EOT ($n\times d$) of $\lambda/4$, and the thickness of central layer is 2λ. The resolution of the grid in digital simulation of reflectance spectrum is set to be 1 nm, and the reflective indexes are determined to be $n_L=n_{Lc}=1.5$ and $n_H=2.1$ by experiment. In Fig.1(b), the resonance wavelength of λ_c is located at 1 390 nm, and the layer thicknesses are $d_H=\lambda_c/(4n_H)=165$ nm, $d_L=\lambda_c/(4n_L)=252$ nm and $d_{Lc}=2\lambda_c/n_{Lc}=1\,854$ nm correspondingly. From the calculated reflectance spectrum of PSM shown in Fig.1(b) following the $(LH)^6L_c(HL)^6$ sequence, we can see that there is a sharp resonance peak in the center of high reflectivity stop band, which means the light is confined in and along the defect channel by omnidirectional reflection band (ORB) from PSM. In electrochemical anodization process, over-numbered anodized layers may destroy the layers near the surface, and the scattering effect in those destroyed layers can decrease the edge quality of stop band, which may give a lower Q factor value[18]. Based on these considerations, we insert three periods of high and low refractive index layers in the center of PSM following $(LH)^5L_c(HL)^5$ sequence. A dual-channel flexible dual-microcavity structure with $(LH)^5\frac{L_c}{2}(HLH)\frac{L_c}{2}(HL)^5$ sequence is formed as shown in Fig.1(c), and the corresponding calculated reflectance spectrum is shown in Fig.1(d). There are two sharp resonant peaks on both sides of the resonance wavelength (λ_c=1 390 nm) appearing in the high reflectivity stop band, which are separately located at 1 336 nm and 1 448 nm in the calculated reflectance spectrum.

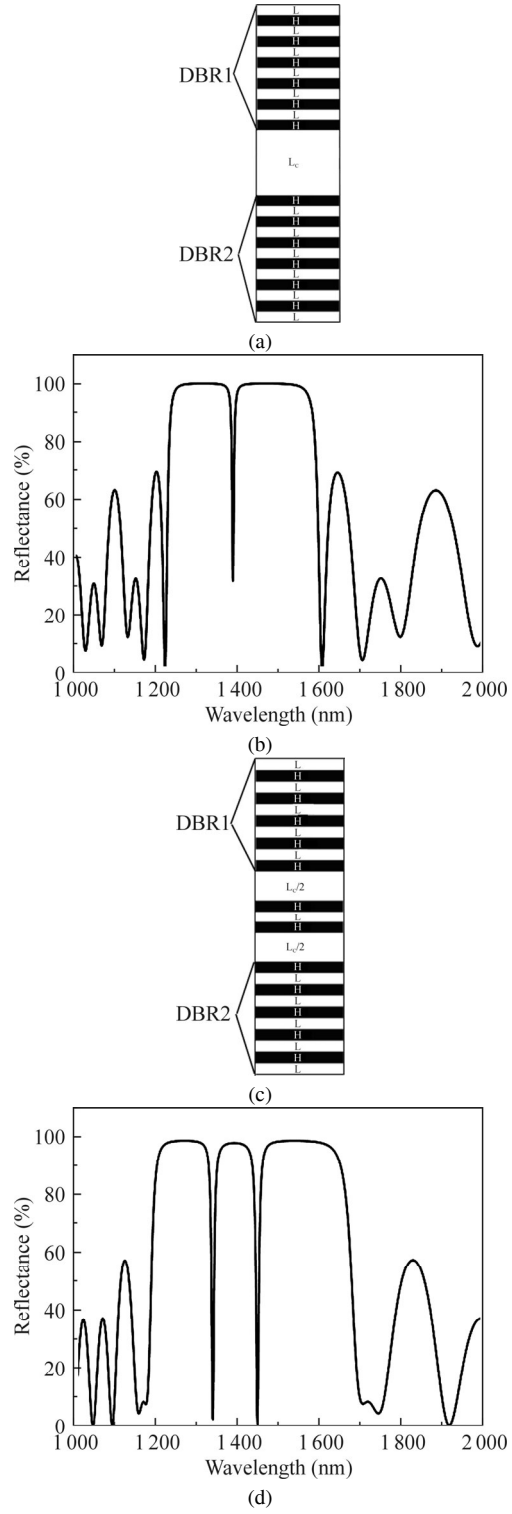

Fig.1 (a) Schematic diagram and (b) calculated reflectance spectrum of PSM following $(LH)^6L_c(HL)^6$ sequence; (c) Schematic diagram and (d) calculated reflectance spectrum of PS dual-microcavity with $(LH)^5\frac{L_c}{2}(HLH)\frac{L_c}{2}(HL)^5$ sequence

PS dual-microcavity samples were prepared from (100) oriented, boron-doped p-type silicon substrate with resistivity of 0.01–0.02 Ω·cm and thickness of 420±10 μm,

and were cut into 2 cm×2 cm squares. Before electrochemical anodization, all pieces were cleaned with carbinol, alcohol and deionized water successively. In the electrochemical anodization process, a mixed solution composed of 49% aqueous hydrofluoric acid and ethanol with a volume ratio of 1:1 was used, and an exposing area is approximately to 0.785 cm^2. In order to obtain 1D photonic crystal structure following $(LH)^5\frac{L_c}{2}(HLH)\frac{L_c}{2}(HL)^5$ sequence, the periodic multilayer structures of PS films were fabricated by using a computer program (Labview) to alternately change current density and etching time in anodization process. There was a 5 s pause after the formation of each layer.

After being etched, all samples were cleaned with deionized water and dried at room temperature in air. Freshly etched PS is unstable in air owing to the "fragile" Si-H bond is easy to be oxidized. In order to get stabilized PS, the freshly etched PS sample needs to be oxidized thoroughly. So the prepared PS samples were soaked in H_2O_2 (30%) for 24 h at room temperature and rinsed thoroughly with deionized water. In this experiment, all the chemicals were of analytical reagent grade.

The thickness and the configuration of samples were performed by Field emission scanning electron microscopy (FESEM, Hitachi, S4800, Japan). The reflectivity spectra of the samples were taken by ultraviolet-visible (UV-vis) spectrophotometer (Hitachi U-4100, Japan), and the reflectivity spectra were obtained in a wavelength range from 400.0 nm to 2 000.0 nm.

The refractive index of silicon-dioxide (SiO_2) is less than that of silicon, and the decrease of refractive index of oxidized PS causes a blue shift in reflectance spectrum. In order to study the difference between spectra of fresh and oxidized PS dual-microcavity samples, we use the transfer matrix method to calculate the reflectance spectra of the dual-microcavity following $(LH)^5\frac{L_c}{2}(HLH)\frac{L_c}{2}(HL)^5$ sequence with the different resonance wavelengths as shown in Fig.2. The calculated resonance wavelength of fresh dual-microcavity at 1 448 nm is shown in Fig.2(a), where the reflective indexes are determined to be n_L=n_{Lc}=1.5 and n_H=2.1 by experiment, and the layer thicknesses are d_H=λ_c/(4n_H)=172 nm, d_L=λ_c/(4n_L)=241 nm and d_L=λ_c/n_{Lc}=965 nm correspondingly. The resonance wavelength of fresh dual-microcavity locates at 1 448 nm, and two sharp resonance peaks in the band gap locate at 1 391 nm and 1 506 nm, respectively, with a width of 115 nm. Considering that the change of refractive index of high porosity of PS is less than of low one after oxidation, we choose the resonance wavelength of oxidized dual-microcavity at 1 385 nm, where the reflective indexes are determined to be n_L=n_{Lc}=1.44 and n_H=2.01 by experiment, and the layer thicknesses are d_H=λ_c/(4n_H)=172 nm, d_L=λ_c/(4n_L)=241 nm and d_L=λ_c/n_{Lc}=965 nm. The calculated reflectance spectrum in the band gap have two sharp resonance peaks located at 1 335 nm and 1 446 nm with a width of 111 nm.

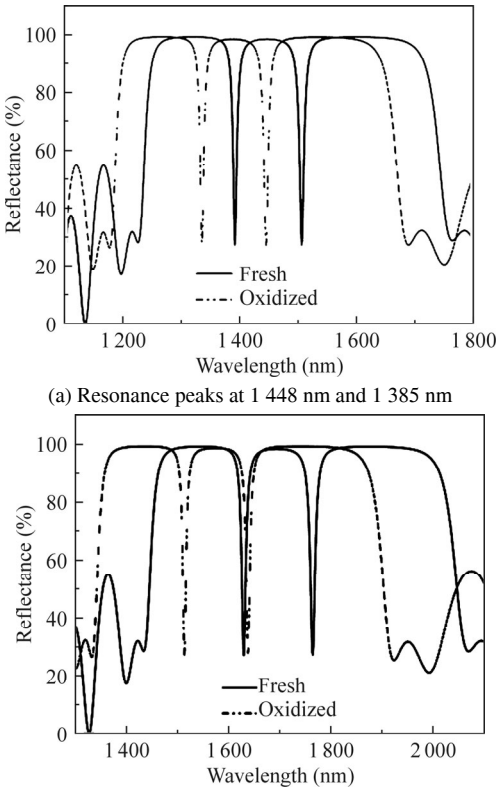

(a) Resonance peaks at 1 448 nm and 1 385 nm

(b) Resonance peaks at 1 695 nm and 1 572 nm

Fig.2 Calculated reflectance spectra of fresh and oxidized PS dual-microcavity following $(LH)^5\frac{L_c}{2}(HLH)\frac{L_c}{2}(HL)^5$ sequence

Fig.3(a) describes a cross-sectional image of the fresh PS dual-microcavity following the $(LH)^5\frac{L_c}{2}(HLH)\frac{L_c}{2}(HL)^5$ sequence with the resonance wavelength of 1 448 nm. The strong contrast between alternate layers of dual-microcavity confirms that a large porosity difference is achieved. The dark gray color PS layers correspond to that with low refractive index (n_L), whereas the light gray color layers correspond to that with high refractive index (n_H). In periodic multilayer structures, two microcavities can be clearly found, which is in accordance with the designed structure shown in Fig.1(c). The thickness of high or low refractive index layer is about 170 nm or 240 nm, and the thickness of microcavity is about 950 nm, which is the same as our simulation. Fig.3(b) shows a surface image of the PS dual-microcavity photonic crystal. The average diameter of the pores is about 15–20 nm, and the distribution is random.

Fig.4(a) shows the measured reflectance spectra of the fresh dual-microcavity following the $(LH)^5\frac{L_c}{2}(HLH)\frac{L_c}{2}(HL)^5$ sequence, in which the resonance wavelength is

1 448 nm, and two sharp resonance peaks locate at 1 506 nm and 1 391 nm, respectively. After oxidization, the resonance wavelength shifts to 1 385 nm, and the two sharp resonance peaks shift to 1 446 nm and 1 335 nm, which are very close to common optical communication wavelengths. By changing the EOT of periodic multi-layer PS, the resonance wavelength moves to 1 695 nm, and the two sharp resonance peaks in the band gap locate at 1 767 nm and 1 628 nm, respectively, as shown in Fig.4(b). After being oxidized, the resonance wavelength shifts to 1 572 nm, and two sharp resonance peaks shift to 1 638 nm and 1 511 nm, respectively. As shown in Fig.4, the reflectance spectrum of oxidized PS dual-microcavity shifts to lower wavelength, resulting from the decrease of the refractive index after PS layer being oxidized. All those results are in good agreement with the calculated reflectance spectra as shown in Fig.2. Based on our experiment, Fig.4(a) shows that there are a blue shift of about 56 nm for the reflectance spectrum of oxidized dual-microcavity at 1 391 nm, a blue shift of 63 nm for the one at 1 448 nm and a blue shift of 60 nm for the one at 1 506 nm. Fig.4(b) shows that there are a blue shift of about 117 nm for the reflectance spectrum of oxidized PS dual-microcavity at 1 628 nm, a blue shift of 123 nm for the one at 1 695 nm and a blue shift of 129 nm for the one at 1 769 nm. It means that the oxidized PS based optical device has a larger blue shift for high wavelength than that for low wavelength.

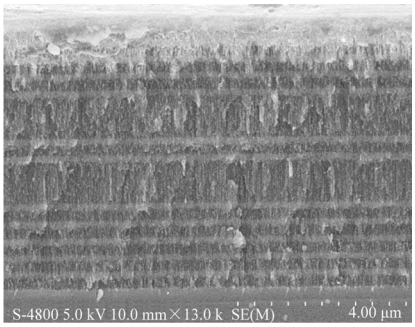

(a)

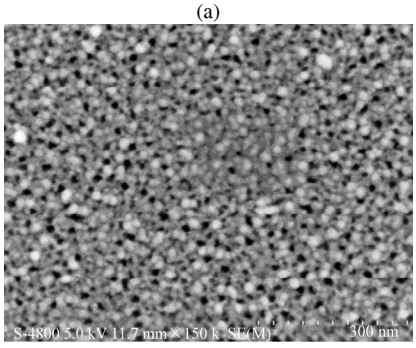

(b)

Fig.3 (a) FESEM cross-sectional image and (b) Top view of the surface of porous silicon dual-microcavity following the $(LH)^5\frac{L_c}{2}(HLH)\frac{L_c}{2}(HL)^5$ sequence

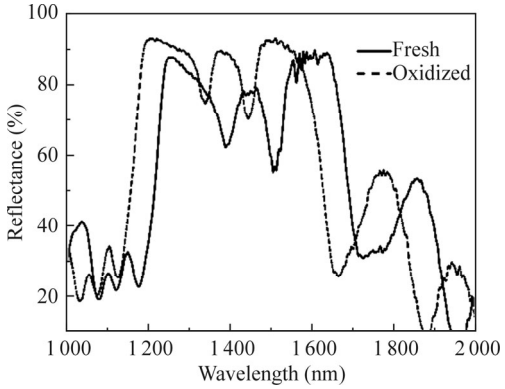

(a) Resonance wavelength at 1 448 nm

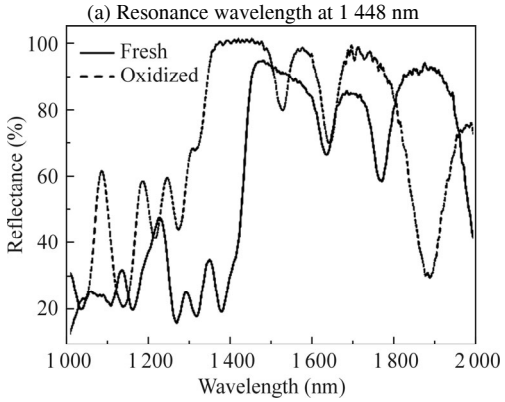

(b) Resonance wavelength at 1 695 nm

Fig.4 Experimentally measured reflectance spectra of fresh and oxidized PS dual-microcavity photonic crystals following the $(LH)^5\frac{L_c}{2}(HLH)\frac{L_c}{2}(HL)^5$ sequence

From the above discussions, we can conclude that the resonance wavelength can be tuned by changing the EOT of each PS layer. Different resonance wavelengths of dual-microcavity have different widths beween two sharp resonance peaks. Oxidization makes the blue shift become larger for high wavelength than that for low wavelength.

By inserting three periods of high and low reflective index layers in the center of PSM, a compact dual-band BPF based on PS dual-microcavity following the $(LH)^5\frac{L_c}{2}(HLH)\frac{L_c}{2}(HL)^5$ sequence is achieved by electrochemical etching. The resonance wavelength can be effectively tuned by changing each EOT of PS layer. Just as expected, the resonance wavelengths of two oxidized resonance peaks are located at 1 335 nm and 1 446 nm, respectively, which are very close to the common optical communication wavelengths. This structure is stable and easy to be prepared, which can be of great potential in realizing integrated optical devices.

References

[1] E. Yablonovitch, Journal of the Optical Society of America B **10**, 283 (1993).

[2] ZHANG Pei-pei, YAO Jian-quan, CUI Hai-xia and LU Ying, Optoelectronics Letters **9**, 342 (2013).
[3] Mohammad Kaleem, ZHANG Xin, YANG You-guang, ZHUANG Yuan and HE Jian-jun, Optoelectronics Letters **9**, 358 (2013).
[4] J. Bao, J. Xiao, L. Fan, X. Li, Y. Hai, T. Zhang and C. Yang, Optics Communications **329**, 109 (2014).
[5] T. F. Khalkhali, B. Rezaei, A. SoltaniVala and M. Kalafi, Optics Communications **326**, 43 (2014).
[6] L. Zhang, D. Yang, K. Chen, T. Li and S. Xia, Optics and Laser Technology **50**, 195 (2013).
[7] G. Lin, X. Chen and D. Zhuang, Optik-International Journal for Light and Electron Optics **125**, 4322 (2014).
[8] M. Y. Mahmoud, G. Bassou and F. Metehri, Optik-International Journal for Light and Electron Optics **125**, 4718 (2014).
[9] A. Saliminia, A. Proulx and R. Vallée, Optics Communications **333**, 133 (2014).
[10] Rui Hu, Yuzhang Liang, Siyu Qian and Wei Peng, Optics Communications **336**, 110 (2015).
[11] N. Barkalina, C. Charalambous, C. Jones and K. Coward, Nanomedicine: Nanotechnology, Biology, and Medicine **10**, 921 (2014).
[12] M. Michał and G. M. Małgorzata, Chemical Engineering Journal **288**, 596 (2013).
[13] K. S. Krishna, Y. Li, S. Li and C. S. S. R. Kumar, Advanced Drug Delivery Reviews **65**, 1470 (2013).
[14] H.Y. Zhang, Z. H. Jia, X. Lv, J. Zhou, L. Chen, R. Liu and J. Ma, Biosensors and Bioelectronics **44**, 89 (2013).
[15] A. Trabelsi and A. Zouari, Solar Energy **107**, 220 (2014).
[16] N. H. Maniy, S. R. Patel and Z. V. P. Murthy, Materials Research Bulletin **57**, 6 (2014).
[17] S. Dhanekar and S. Jain, Biosensors and Bioelectronics **41**, 54 (2013).
[18] L. J. Adam, G. S. Adrian, S. Adnan, J. S. Michael and M. M. Gordon, Sensors & Actuators: A. Physical **203**, 154 (2013).